D. Dietzel, D. Messig, F. Piscaglia, A. Montorfano, G. Olenik, O.T. Stein, A. Kronenburg, A. Onorati, C. Hasse
Evaluation of Scale Resolving Turbulence Generation Methods for Large Eddy Simulation of Turbulent Flows
Computers & Fluids, Vol. 93, 2014, p. 116-128
doi:10.1016/j.compfluid.2014.01.013

Evaluation of scale resolving turbulence generation methods for Large Eddy Simulation of turbulent flows

Dirk Dietzel[a], Danny Messig[*,a], Federico Piscaglia[b], Andrea Montorfano[b], Gregor Olenik[c], Oliver T. Stein[c], Andreas Kronenburg[c], Angelo Onorati[b], Christian Hasse[a]

[a] *Chair of Numerical Thermo-Fluid Dynamics, ZIK Virtuhcon, TU Bergakademie Freiberg, Fuchsmühlenweg 9, 09599 Freiberg, Germany*
[b] *Energy Department, Politecnico di Milano, via Lambruschini 4, 20156 Milano, Italy*
[c] *Institut für Technische Verbrennung, Universität Stuttgart, Herdweg 51, 70174 Stuttgart, Germany*

Abstract

Large Eddy Simulation (LES) has become an attractive simulation method even for technical processes and it usually provides space and time resolved fluctuations of a significant portion of the spectrum. However, in contrast to a RANS simulation an accurate LES requires the definition of suitable initial and boundary conditions, which includes turbulent structures with physically sound spatial and temporal correlations. Such turbulent structures are usually generated artificially at the boundary. Three different algorithms for generating turbulent fluctuations are evaluated in the present work. The investigated methods are Filtered noise (Klein et al. Klein et al. [2003]), Diffused noise (Kempf et al. Kempf et al. [2005]) and an Inverse Fourier approach (Billson Billson et al. [2003], Davidson Davidson [2007a]). These techniques were developed for generating inflow data for LES and have already been used in published research Bordas et al. [2012], Bini and Jones [2008], Kuenne et al. [2012], Enjalbert et al. [2012], Duwig [2011], Rhea et al. [2009], Olbricht et al. [2012], Pettit et al. [2011], Fru et al. [2011], Stein et al. [2011], Piscaglia et al. [2013], e.g. for investigating turbulent combustion processes. In the present work the turbulent statistics i.e. energy spectra and velocity correlations as well as derived quantities such as turbulent kinetic energy and subgrid scale viscosity are investigated in more detail in a comparative fashion for the generated turbulent velocity fields. As a simple test case, the decay of turbulence in a cubical box, is considered here to provide information on the initially generated turbulence as well as its temporal evolution.

[*]Corresponding author
Email address: danny.messig@iec.tu-freiberg.de (Danny Messig)

The results are analyzed in detail and are compared to experimental data. Turbulence fluctuations generated by Filtered noise and Diffused noise lead to similar results. The resulting energy spectra and velocity correlations agree generally well with experimental data despite some discrepancies at very early times after initialization. The Inverse Fourier approach yielded good agreement at all times, but at increased computational cost. In addition, the implementation of Filtered noise and Diffused noise might be easier for most cases of practical interest. In particular, the Diffused noise approach can be used for the generation of inhomogeneous turbulence on arbitrary grids.

Key words: Inlet boundary, Turbulence Generation, LES, Turbulent boundary condition

---

Nomenclature

C_s Smagorinsky constant

CFD Computational Fluid Dynamics

Co Courant number

D diffusion coefficient

DN Diffused Noise

$\mathcal{D}$ dissipation of turbulent kinetic energy

E specific kinetic energy

f longitudinal velocity correlation

FN Filtered noise

FT Fourier transform

g transverse velocity correlation

HIT homogeneous isotropic turbulence

IF Inverse Fourier approach

k turbulent kinetic energy

L_{int} longitudinal integral length scale

M size of active grid

M_i number of elements of simulation domain

NRC numerical reference case

$\mathcal{P}$ production of turbulent kinetic energy

r separation distance between correlated points

R auto-correlation function

$\mathcal{R}$ random number

$RANS$ Reynolds averaged Navier-Stokes

$S_{i,j}$ strain rate

t time

$\mathcal{T}$ rate of transfer of turbulent kinetic energy

u_i velocity

u_{rms} root-mean-square velocity

$\delta_{i,j}$ Kronecker delta

Δ filter width

ε dissipation rate

ϕ phase of Fourier mode

κ_j wave number vector

κ_e wave number of most energetic scales

κ_{kol} wave number of most dissipative scales

ν kinematic viscosity

σ_i direction of Fourier mode

τ integral time scale

$\tau_{i,j}$ stress tensor

η Kolmogorov length scale

$\langle\rangle$ time average

1. Introduction

Turbulent fluid motion plays a central role in most flow configurations of technical interest and it introduces special requirements for their simulation. One possibility to capture turbulent fluctuations is the use of Large Eddy Simulation (LES) providing a partially space and time resolved solution at moderate computational effort. Depending on the grid and time resolution, a significant portion of the turbulent spectrum is resolved and this (also considering the coupling of turbulence with other processes such as combustion) usually leads to more predictive simulations when compared to RANS approaches.

A crucial element of any numerical simulation is the definition of proper boundary conditions. The suitability of the prescribed physical quantities at the domain boundaries is essential for getting accurate results. Since in LES turbulent structures are resolved both in space and time, the velocity field at the inlet has to contain space and time dependent fluctuations superimposed on the mean velocity. These fluctuations have to be physically meaningful making the definition of inflow boundary conditions a challenging task. The spectral content of the velocity signal and the spatial and temporal correlation of the eddies are two characteristic properties, which have to be satisfied. Different techniques for generating turbulent data at the inflow plane of the simulation domain were developed to fulfill the requirements of turbulent inflow conditions Klein et al. [2003], Kempf et al. [2005], Davidson [2007a], Huang et al. [2010], Jarrin et al. [2006], Montomoli and Eastwood [2011], Baba-Ahmadi and Tabor [2009]. Performing an auxiliary simulation is one possible way of defining suitable inflow turbulence. The simulation domain is extended upstream from the inlet to allow the turbulence to develop naturally. The additional computational effort, which increases the cost and time of the whole simulation is the main drawback of this procedure Kempf et al. [2005]. Another possibility is to artificially generate turbulent fluctuations. In this context one way is to apply an inverse Fourier transform on a predefined energy spectrum function Lee et al. [1992], Sohm [2007]. The velocity can then be determined from the calculated Fourier coefficients. This

algorithm is used for validating the numerical setup in Sec. 4.1. The method generates velocity fields which satisfy a desired energy spectrum and continuity, but the algorithm is difficult to implement, particularly for anisotropic turbulence Klein et al. [2003] or arbitrary grids. A comparative study of different inflow boundary conditions including recycling and rescaling as well as precursor-like approaches was presented by Pronk and Hulshoff Pronk and Hulshoff [2012]. The algorithms were applied and evaluated for a boundary layer flow on a flat plate. A detailed review on different techniques for the generation of turbulence at inlet boundaries was presented by Tabor and Baba-Ahmadi Tabor and Baba-Ahmadi [2010].

For the present work three different methods for generating artificial turbulence - proposed by Klein et al. Klein et al. [2003], Kempf et al. Kempf et al. [2005] as well as Billson Billson et al. [2003] and Davidson Davidson [2007a] - are investigated in more detail. The approach of Klein et al. Klein et al. [2003] is based on digital filtering of random data and is referred to as Filtered noise (FN). Kempf et al. Kempf et al. [2005] diffuse random noise to obtain correlated turbulent structures. Hence the algorithm is denoted Diffused noise (DN) in the following. The turbulence generation method proposed by Billson and Davidson is based on random Fourier modes of a prescribed energy spectrum. The algorithm is designated Inverse Fourier approach (IF) in the remainder of this text. These algorithms were developed for generating turbulent inflow data and have widely been used in research on different issues ranging from flame modeling in gas turbines to turbulent jet flows. Several examples of their application are found in Bordas et al. [2012], Bini and Jones [2008], Kuenne et al. [2012], Enjalbert et al. [2012], Duwig [2011], Rhea et al. [2009], Olbricht et al. [2012], Pettit et al. [2011], Fru et al. [2011], Stein et al. [2011], Piscaglia et al. [2013]. However the characteristics of the generated turbulence has not been investigated in detail yet. Knowing the properties of the turbulent inflow data, such as spectral content, can improve the understanding of problems, which might occur in the simulation. E.g. the dissipation of turbulent kinetic energy strongly depends on the velocity gradients of the smallest resolved length scales. If an artificially generated turbulence field does not contain eddies at these scales the dissipation will be underpredicted considerably. Thus the aim of the present work is to investigate the quality of the three algorithms with respect to the following issues:

- Does the generated velocity field fully represent the characteristic energy spectrum for homogeneous isotropic turbulence (HIT)?
- Does the generated velocity field reproduce physically correct longitudinal and

transverse velocity correlations?

- How do the turbulent properties develop in time during the decay of turbulence in a box?
- Which characteristics of the different algorithms have to be considered for their application?

2. Fundamentals

2.1. Simulation theory

For the present analysis it suffices to consider constant property flows at low Mach numbers. Then, the conservation equations for mass and momentum reduce to Versteeg and Malalasekera [2007]

$$\frac{\partial u_i}{\partial x_i} = 0 \tag{1}$$

and

$$\frac{\partial u_j}{\partial t} + \frac{\partial u_i u_j}{\partial x_i} = -\frac{1}{\rho}\frac{\partial p}{\partial x_j} + \frac{\partial}{\partial x_j}\left(\nu \frac{\partial u_i}{\partial x_j}\right) \tag{2}$$

where u, p, ρ and ν are velocity, pressure, density and kinematic viscosity, respectively. For the present investigation LES are performed where these equations are spatially filtered in order to separate larger and smaller length scales. Those smaller length scales, which are not resolved directly have to be considered by subgrid scale closure. In this context the standard Smagorinsky model is one of the most frequently used approaches. It is based on Boussinesq's hypothesis of the eddy viscosity, which describes a proportionality between Reynolds stresses and the strain rate of the resolved velocity field Versteeg and Malalasekera [2007]. In principle the idea of this model is to artificially increase the laminar viscosity ν by the turbulent (subgrid scale) viscosity ν_{sgs} to an effective viscosity ν_{eff}, which increases the friction on the resolved scales. For modeling the subgrid scale viscosity the approach of Prandtl's mixing length model is used leading to the formulation Fröhlich [2006]:

$$\nu_{\text{sgs}} = (C_s\Delta)^2|\overline{S}| = (C_s\Delta)^2\sqrt{2\overline{S}_{i,j}\overline{S}_{i,j}}. \tag{3}$$

where $\overline{S}_{i,j}$ indicates the filtered, resolved part of the shear rate which reads for incompressible flow

$$\overline{S}_{i,j} = \frac{1}{2}\left(\frac{\partial \overline{u}_i}{\partial x_j} + \frac{\partial \overline{u}_j}{\partial x_i}\right). \tag{4}$$

C_s denotes the Smagorinsky model constant. It has to be defined individually for the considered problem with respect to the physical and numerical setup of the simulation in order to induce the correct amount of additional dissipation. It is important to note that since we consider incompressible flow, a solenoidal velocity field is enforced and no compressible fluctuations are accounted for, which is a valid assumption for the case considered below.

2.2. Inflow Generation

2.2.1. Filtered noise - FN

As discussed in the introduction resolving turbulent eddy structures spatially and temporally requires inflow boundary conditions, which fulfill turbulent characteristics. The first algorithm considered for the generation of turbulent velocity fields was introduced by Klein et al. Klein et al. [2003] and is based on digital filtering of random noise. This is expressed as

$$u_m = \sum_{n=-N}^{N} b_n \mathcal{R}_{m+n} \tag{5}$$

where the filter coefficients b_n depend on a prescribed autocorrelation function. u_m is the signal obtained from filtering the random numbers $\mathcal{R}_{m+n}$. The filter coefficients can be derived from

$$\frac{\langle u_m u_{m+k}\rangle}{\langle u_m u_m\rangle} = \left(\sum_{j=-N+k}^{N} b_j b_{j-k} \Big/ \sum_{j=-n}^{N} b_j^2\right) = R. \tag{6}$$

The autocorrelation function R used for defining the filter coefficients is estimated as Batchelor [1953]

$$R = \exp\left(-\frac{\pi r^2}{4L_{\text{int}}^2}\right). \tag{7}$$

where r and L_{int} are the distance between correlated points and the integral length scale, respectively. This procedure can easily be extended to three-dimensional space by combining three one-dimensional filters as $b_{i,j,k} = b_i \cdot b_j \cdot b_k$. The such obtained signal is finally scaled according to Lund et al. Lund et al. [1998] to obtain velocity fluctuations matching a pre-defined Reynolds stress tensor. For generating three-dimensional turbulence fields the following steps have to be performed:

- Initialize one random field per velocity component. In each direction they have to contain $M_i + 2N_i$ elements where M_i and N_i are the number of elements of the computational mesh and the filter width in each coordinate direction, respectively. It is recommended to choose the filter width such that we capture twice the desired integral length scale. This ensures sufficient filtering at moderate computational cost.

- After determining the filter coefficients b_n each random field has to be filtered according to Kempf et al. [2012]

$$\mathcal{R}^{\text{fil}}(i,j,k) = \sum_{i'=-n_x}^{n_x} b_x(i',j',k') \sum_{j'=-n_y}^{n_y} b_y(i',j',k') \sum_{k'=-n_z}^{n_z} b_z(i',j',k') \mathcal{R}(i+i',j+j',k+k'). \tag{8}$$

- Normalize the filtered signal such that the resultant field has zero mean and a variance of 1.

- Apply Lund's transformation, which reads:

$$u_i = \bar{u}_i + a_{i,j} \mathcal{R}_j^{\text{fil}}, \tag{9}$$

with

$$a_{i,j} = \begin{pmatrix} \langle u_1' u_1' \rangle^{1/2} & 0 & 0 \\ \langle u_2' u_1' \rangle / a_{11} & (\langle u_2' u_2' \rangle - a_{21}^2)^{1/2} & 0 \\ \langle u_3' u_1' \rangle / a_{11} & (\langle u_3' u_2' \rangle - a_{21} a_{31}) / a_{22} & (\langle u_3' u_3' \rangle - a_{31}^2 - a_{32})^{1/2} \end{pmatrix}. \tag{10}$$

- The scaled fluctuations can finally be copied to the simulation domain.

Since the actual scope of FN is to produce inflow data, Klein et al. Klein et al. [2003] presented a modified algorithm creating two-dimensional slices of velocity fields at each time step which were also temporally correlated.

2.2.2. Diffused noise - DN

In a similar way the algorithm proposed by Kempf et al. Kempf et al. [2005] creates fluctuations at a prescribed length scale and rms-level. Here, the filtering procedure is simply replaced by a diffusion process according to

$$\frac{\partial \mathcal{R}_i}{\partial t} = D \frac{\partial^2 \mathcal{R}_i}{\partial x_j^2} \tag{11}$$

which yields growing integral length scales, similarly as obtained from a filtering operation. The diffusion time t_{dif} can be derived from

$$L_{\mathrm{int}} \approx \sqrt{2\pi D t_{\mathrm{dif}}} \tag{12}$$

depending on the desired integral length scale with the diffusion coefficient D. Kempf et al. Kempf et al. [2005] found that the velocity correlations created by diffusion of random noise satisfy the model correlation in Eq. (7). Again Lund's transformation Lund et al. [1998] is finally applied in order to capture the desired Reynolds stress tensor. In contrast to FN this algorithm is not limited to equidistant meshes and can be applied to arbitrary geometries. Hence the diffusion process can directly be performed on any computational mesh.

2.2.3. Inverse Fourier approach - IF

Billson Billson et al. [2003] and Davidson Davidson [2007a] presented another algorithm for generating turbulent velocity fields, which is principally based on the work of Kraichnan Kraichnan [1970]. Here, the velocity signal is obtained from a specified number N of random Fourier modes (typically 150 to 600) and can be calculated as

$$u_i'(x_j) = 2 \sum_{n=1}^{N} \hat{u}^n \cos(\kappa_j^n x_j + \psi^n) \sigma_i^n, \tag{13}$$

where $\hat{u}^n$, ψ^n and σ_i^n are the amplitude, phase and direction of the n-th Fourier mode, respectively. The wave number vector κ_j^n describes the size of an eddy in

wave number space. The steps necessary for the definition of accurate fluctuations are summarized as follows:

- The random angles φ^n, θ^n, α^n and ψ^n have to be defined for each Fourier mode n.
- The highest wave number has to be determined according to the mesh resolution as $\kappa_{\max} = \pi/\Delta x$. The lowest wave number depends on the wave number of the most energetic length scales κ_e as $\kappa_{\min} = \kappa_e/p$ with $p > 1$ and $\kappa_e = 9\pi A/(55L_{\text{int}})$ where $A = 1.4256$ is a constant. The wave number space ranging from $\kappa_{\min}$ to $\kappa_{\max}$ can then be divided into $N-1$ modes of the same size $\Delta\kappa$.
- For each mode n the wave number vector κ_j^n has to be defined according to Fig. 1. The magnitude $|\kappa_j^n|$ is determined by $|\kappa_j^n| = \kappa_{\min} + (n-1)\cdot\Delta\kappa$. In order to ensure continuity the unit vector σ_i has to be orthogonal to κ_j.
- Now the amplitudes $\hat{u}$ can be determined for each Fourier mode as

$$\hat{u}^n = \sqrt{E(|\kappa_j^n|)\cdot\Delta\kappa}, \tag{14}$$

  according to a modified von-Kármán spectrum that is given by

$$E(|\kappa_j|) = \frac{A\cdot u_{\text{rms}}^2}{\kappa_e}\frac{\left(\frac{|\kappa_j|}{\kappa_e}\right)^4}{\left[1+\left(\frac{|\kappa_j|}{\kappa_e}\right)^2\right]^{17/6}}\cdot e^{-2\left(\frac{|\kappa_j|}{\kappa_{\text{kol}}}\right)^2}. \tag{15}$$

  The wave numbers κ_e for most energetic and κ_{kol} for most dissipative eddies as well as the root-mean-square velocity u_{rms} have to be prescribed according to the desired turbulent statistics. Evaluating Eq. (15) with κ_j^n for each Fourier mode gives the corresponding spectral energy E.
- For every face of the inlet patch $\hat{u}^n$, κ_j^n, ψ^n and σ_i^n can finally be inserted into Eq. (13) leading to the velocity fluctuation $u_i'(x_j)$.

The Fourier series in Eq. (13) has to be applied at each time step where temporal correlation is created applying a Billson filter on two subsequent time steps Davidson

[2007a]. Moreover damping functions for free stream turbulence and near wall treatment are proposed by Davidson Davidson [2007b]. Since for the present investigation only turbulence generation in a cubical box is considered both the Billson filter and the damping functions do not apply here. Instead the procedure is applied for every mesh cell to generate a three dimensional velocity field.

2.2.4. Comparison of the proposed inflow generation methods

The three presented inflow generation methods differ in their basic idea of creating turbulent structures. Hence the parameters to be prescribed and the limitations of the algorithms differ as well. Some comments on the properties of the different methods should be given at this point. Each algorithm requires the turbulent length scale L_{int} (in IF in terms of the corresponding wave number) and the intensity of the fluctuations. For FN and DN these values can be chosen for each coordinate direction independently allowing for the generation of anisotropic turbulence. For IF the Kolmogorov length scale has to be prescribed in addition. It is determined from the viscosity of the fluid and the dissipation rate ε. The latter can easily be estimated as $\varepsilon \approx u_{\text{rms}}^3/L_{\text{int}}$ Pope [2000], so that actually no additional information is required. Damping of the turbulent fluctuations in the vicinity of solid boundaries or in the far field of a free stream with appropriate blending functions is proposed by Davidson Davidson [2007b]. This procedure can easily be applied to the FN and DN algorithm, too. When using FN or IF the fluctuations can be generated at each time step on the fly. For the diffusion of the random noise, as it is presented in Kempf et al. [2005], at first a three-dimensional fluctuation field has to be generated. By applying Taylor's hypothesis single slices of this field can then be copied to the inflow plane enabling an on-the-fly simulation as well.

3. Numerical setup

The test case of decaying homogeneous isotropic turbulence is a popular choice for investigating the quality of newly developed turbulence models or simulation techniques, used e.g. in Moin et al. [1991], Fureby et al. [1997], Nicoud and Ducros [1999], Hasse et al. [2009], Nicoud et al. [2011]. Here, the temporal evolution of HIT at $Re_\lambda = 71.6$ is studied, where $Re_\lambda = \frac{u_{\text{rms}} \cdot \lambda}{\nu}$ is the Taylor Reynolds number based on the Taylor micro scale λ Pope [2000]. The simple geometry and the low Reynolds number make it possible to resolve even the smallest scales at moderate computational cost Sohm [2007]. Here, we use this test case for investigating turbulent characteristics, which are obtained using the different turbulence generators. We evaluate the numerical results from the three different generators by comparing them to the experimental data of Comte-Bellot and Corrsin Comte-Bellot and

Corrsin [1971]. They measured turbulent statistics at three different downstream positions in a wind tunnel. The initial conditions for the numerical simulations were set according to the first downstream position in the experiments. Hence, by applying Taylor's hypothesis the three locations correspond to dimensionless times of $\tilde{t} = 0$, $\tilde{t} = 56$ and $\tilde{t} = 129$ where $\tilde{t} = \frac{U_0 \cdot t}{M}$ with $U_0 = 10$ m/s and $M = 0.0508$ m, where M is the size of the active grid, which was used for generating a well defined turbulence field in the experiments. In Tab. 1 the initial data for generating the three-dimensional turbulence fields are listed. The setup using homogeneous isotropic turbulence shall be understood as a first step towards our understanding of the effect of the turbulence generation methods on the further evolution of the flow field. Additional test cases (e.g. shear flows and arbitrary grids) should complement the present study in the future and should provide a corroboration or guidelines for desired modifications of the findings presented in Section 4.

The cubical simulation domain, which is initialized with turbulent fluctuations with a zero mean velocity has an edge length of $L = 10 \cdot M = 0.508$ m. Three different equidistant computational meshes were created containing 64^3, 128^3 and 256^3 cells, respectively. These meshes will be referred to as grid I, grid II and grid III in the following. Cyclic boundary conditions were applied at each boundary plane of the cube. Subgrid scale closure is achieved using a standard Smagorinsky model. According to Sohm [2007] the CFL-criterion for determining the time step size is $Co \leq 0.1$. The grid and time spacing for the different computational meshes is shown in Tab. 2. The three considered inflow generators (FN, DN, IF) are used for initializing three-dimensional HIT fields. A validation of the overall numerical setup is accomplished by using a full, inverse Fourier transform of a von-Kármán-Pao model spectrum to initialize the velocity fields. It is denoted as numerical reference case (NRC) in the following. This procedure is similar to the IF approach presented in Sec. 2.2.3. The main difference is found in the representation of the Fourier series, which reads:

$$u_i'(x_j) = 2 \sum_{\kappa_j} \hat{u}(\kappa_j) \sigma_i(\kappa_j) e^{i \kappa_j \cdot x_j}. \tag{16}$$

By using IF a certain number N of wave number vectors with random spatial orientation in wave number space is defined. For the numerical reference case one wave number vector for each cell of the computational mesh is defined in order to contain all possible wave number vectors existing for the grid. The computational effort of the latter method increases strongly with mesh resolution due to performing a summation for each cell over the total number of cells. Applying a Fast Fourier transform

distinctly speeds up the calculation limiting the procedure to meshes containing 2^n cells. This makes the algorithm difficult to apply for arbitrary boundary patches. The suitability of the proposed algorithm to create velocity fields accurately representing a specific energy spectrum is pointed out in Sec. 4.1. The IF approach is a simplification of this algorithm, which can be applied to boundary patches more easily.

Air at standard conditions is considered in the present case. A test of different discretization schemes revealed no significant differences between first and second order time discretization for the present setup as can be seen in Fig. 2. Here, we used a first order Euler scheme and a second order Crank-Nicolson (CN) scheme that yielded very similar results in terms of the decay of the energy spectrum even for the highest wave numbers. Since the computational effort is considerably lower for the Euler scheme when compared to the CN scheme and since the additional numerical dissipation of the Euler scheme does not seem to affect the small scales in our computations, a first order Euler implicit scheme is used for time integration whereas a second order central differencing scheme is used in space.

The OpenFOAM® toolbox version 2.1 was used for performing the different simulations. The inflow generators were integrated into the OpenFOAM® framework by the research groups from Freiberg (FN), Stuttgart (DN) and Milan (IF). The Navier-Stokes equations are solved using pisoFoam, which is suitable for the simulation of transient, incompressible flow and provides incorporation of turbulence modeling.

4. Results

4.1. Numerical reference case - NRC

Figure 3 depicts the energy spectra obtained from the flow field initialized by an inverse Fourier transform. Observing the graphs at $\tilde{t} = 0$ it is seen that the model spectrum of the initialized velocity field matches the experimental data well. On every computational mesh simulations using different Smagorinsky constants were performed. Best agreement comparing numerical and experimental data is obtained choosing $C_s = 0.17$ on grid I and $C_s = 0.14$ on grid II and grid III and these values were used for all subsequent calculations. It has to be noted that this procedure to determine C_s is meant to ensure the correct decay, which is governed both by physical and numerical dissipation. However, the obtained Smagorinsky constants are well within the usually applied range.

The decay of the turbulent kinetic energy k is illustrated in Fig. 4. The resolved kinetic energy k_{res} and the total kinetic energy k_{tot} summed up from k_{res} and subgrid scale energy k_{sgs} are plotted against time. The resolved part can simply be evaluated by integrating the energy spectra over all wave numbers at every time step. The subgrid scale kinetic energy is estimated by

$$k_{\mathrm{sgs}} = \frac{2c_k}{c_e}\Delta^2|\overline{S}_{i,j}|^2. \tag{17}$$

from within the Smagorinsky model in OpenFOAM® with $c_k = 0.094$ on grid I and $c_k = 0.0727$ on grid II and grid III as well as $c_e = 1.0$ for all meshes. The mesh depending values of c_k are directly correlated to the Smagorinsky constant C_s which was adapted as discussed before. The diagram on the left hand side depicts an obvious lack in kinetic energy on the resolved scales for the first time step compared to experiments. The reason is found in the wide range of length scales, which are not resolved on grid I. The Smagorinsky model does not provide a sufficient amount of additional subgrid scale energy leading to an underestimation of the total kinetic energy. For grid II and grid III the resolved energy increases and the subgrid scale kinetic energy decreases compared to grid I, as can be seen from the two simulation lines increasingly approaching each other with increasing grid resolution. The experimental data at $\tilde{t} = 0$ are matched more closely with increased grid resolution. For all computational meshes considered the kinetic energy converges to the experimental data for later times. It is pointed out that the dissipation rate is underestimated since the kinetic energy was underpredicted at the beginning. Especially in the first part of the simulation the kinetic energy decreases too slowly. Even setting $C_s = 0.25$ does not significantly increase the dissipation of k whereas the specific energy at small length scales is strongly underpredicted at this C_s value. It has to be kept in mind that it is difficult to accurately predict the correct decay rate with the employed rather simple standard Smagorinsky model used here.

Figure 5 shows the longitudinal correlation functions for each computational mesh. They are plotted at the same instants in time as the energy spectra. For small r/M the correlation functions are overestimated at $\tilde{t} = 0$. On grid I the characteristic behavior of growing velocity correlations is well captured although not matching the experimental data perfectly. It has to be considered that the integral length scales are not sufficiently resolved on grid I. Hence the results are only taken for estimating the grid dependency. For grid II and grid III it is obvious, that the longitudinal correlation does not grow at the same level as observed in the experiments.

These results are similar to those presented in Sohm [2007]. Comparing numerical and experimental results reveals underpredicted growth rates but basically physical behavior can be observed. Similar results are obtained for transverse correlations (not shown). Overall, the employed LES solver gives good results for the reference case using a von-Kármán-Pao model spectrum as initial condition and this is the basis for the following comparisons of the different turbulence generation mechanisms.

4.2. Filtered noise and Diffused noise

For initializing the velocity field by means of FN and DN the only input parameters to be defined are the integral length scale L_{int} and the Reynolds stresses $\langle u_i' u_j' \rangle$. The normal stresses are defined as $\langle u_i'^2 \rangle = u_{\text{rms}}^2 \approx 0.05\ \text{m}^2/\text{s}^2$. The anisotropic part of the correlation tensor is set to zero. The integral length scale for each direction is defined as $L_{\text{int}} = 0.024$ m.

In Fig. 6 the energy spectra are plotted for both inflow generators and for each grid. The energy spectra of the initialized HIT fields (at $\tilde{t} = 0$) match well with the experiments for the largest scales. In the range of the integral length scales and in the low wave-number range of the inertial subrange too much kinetic energy is induced by both inflow generation methods. In the high wave-number range of the inertial subrange as well as in the dissipation range (if it is resolved) the experimental spectrum is strongly underpredicted. In addition, oscillations can be observed in the high wave number range for the initial conditions generated by the FN approach. They arise from (1) a rather coarse resolution of the filter kernel and (2) the arbitrary boundary conditions used, i.e. periodic boundary conditions are not enforced. In particular the latter favours the occurence of the artificial oscillations. Alleviating both deficiencies would significantly increase the computational cost and complexity. Moreover, it has to be considered that periodicity does not apply for most applications of practical interest, e.g. chambers with walls. In addition, Fig. 6 demonstrates that the oscillations at the high wavenumber end do not unduly influence the subsequent evolution of the turbulent spectrum, and the procedure suggested here provides a good compromise between an accurate representation of the initial conditions, a more universal applicability and the computational cost. It is noted that FN and DN do only provide turbulence with an energy overprediction at the integral length scales whereas almost no small scale eddies are generated. This discrepancy vanishes during the decay of turbulence. A transition from artificially generated turbulence to physical turbulence in the context of HIT can be detected investigating the spectral content of the flow field at later simulation times. For all cases considered in Fig. 6

the shape of the energy spectra becomes closer to physically reasonable profiles at the dimensionless times $\tilde{t} = 56$ and $\tilde{t} = 129$. The limitation to only create large scale turbulence becomes more significant with increasing mesh resolution because smaller scales could actually be resolved on finer meshes. Comparing the dimensionless times $\tilde{t} = 0$ and $\tilde{t} = 56$ it is seen that the kinetic energy increases at the smallest scales for increasing time. This can be explained by means of the balance equation for the specific turbulent kinetic energy Pope [2000]:

$$\frac{\partial E(\kappa, t)}{\partial t} = \mathcal{P}(\kappa, t) - \frac{\partial \mathcal{T}(\kappa,t)}{\partial \kappa} - \mathcal{D}(\kappa, t). \tag{18}$$

$\mathcal{P}(\kappa, t)$, $\mathcal{T}(\kappa,t)$ and $\mathcal{D}(\kappa, t)$ indicate production, transport and dissipation rate of the kinetic energy, respectively. Due to the energy overprediction at the large scales the amount of energy transported from the larger scales is greater than the amount of energy transported to the smaller scales. Hence the gradient of the transport term becomes negative in the range of the smaller resolved length scales. Considering the inertial subrange, where the dissipation term can be neglected, the right hand side of Eq. (18) becomes positive then. During the process of eddy decay the velocity field reaches a physical state containing eddies from the largest to the smallest resolvable scales. Since no additional kinetic energy is produced the excess at the large scales is removed and the small scale eddies transport energy to even smaller scales, which makes the right hand side of Eq. (18) negative in the inertial subrange. Hence the specific energy decreases as can be seen comparing times $\tilde{t} = 56$ and $\tilde{t} = 129$ in Fig. 6. As similar observation can be made on grid III where the dissipation range is partially resolved. It is argued that the transport term exceeds the dissipation term even in the dissipation range of the energy spectrum until reaching the equilibrium state.

In Fig. 7 the temporal evolution of the turbulent viscosity is depicted. It is seen that it strongly depends on the grid resolution. As discussed before the initialized velocity fields contain eddies up to the integral length scales whereas an obvious lack of kinetic energy can be found at the finest resolved scales (Fig. 6). This effect becomes more significant for increasing mesh resolution. Since there are no small scale eddies for FN and DN the velocity gradients are smaller than for the reference case (see also Fig. 10). Considering Eq. (3) this results in a smaller turbulent viscosity. Through decay of large scale eddies smaller ones are generated resulting in increasing shear rates and hence in an increasing turbulent viscosity peaking at dimensionless times $\tilde{t} = 50$ and $\tilde{t} = 60$ on grids II and III, respectively. After reaching the maximum the subgrid scale viscosity decreases approximately at the same level as seen

for the reference case. The time needed for converging to the reference case increases with increasing grid resolution since the characteristic energy cascade has to develop further down to smaller scales. It is concluded that the time needed for achieving a physically correct velocity field in terms of fully resolved energy spectrum increases with increasing grid resolution.

The subgrid scale viscosity affects the rate of dissipation of the turbulent kinetic energy. The evolution of k in time for the three computational meshes is shown in Fig. 8. The results for the two inflow generators are compared to the experimental data and to the results of the numerical reference case. The initialized kinetic energy is overpredicted compared to the experimental data and to results from NRC for grid I. With increasing mesh resolution the overprediction vanishes. For grid II and grid III the kinetic energy of the initialized velocity fields lies in the range of the experimental data and the data from the reference case. It is shown that the kinetic energy is mostly induced at the large scales for FN and DN (Fig. 6). Thus the resolved part of k is nearly constant on grid I, grid II and grid III. The additional subgrid scale kinetic energy, which rises with increasing mesh spacing leads to an overprediction of k_{tot} on grid I (Fig. 8). For the NRC the resolved part of k decreases with increasing mesh spacing. The algorithm provides the distribution of the total kinetic energy on all length scales of the prescribed energy spectrum. The kinetic energy of the smaller length scales, which cannot be resolved on the computational mesh directly (k_{sgs}) is then missing in the initialized HIT field. The gap has to be closed by the LES model. For all three meshes it is observed that there is a significant loss in kinetic energy at the first time steps, which leads to an underprediction of the kinetic energy. Since the initialized velocity fields are not divergence free, continuity is enforced by the pressure correction of the numerical solver in the first time steps, which yields the loss in kinetic energy. For the present case this loss is in the range of 35% of the total kinetic energy at $\tilde{t} = 0$ and is independent of grid resolution. This appears high but it is pointed out that k_{tot} converges to the level of the reference case for grids I, II and III. The initially low turbulent viscosity leads to a low dissipation of k_{tot} particularly on finer meshes. Because of that, the strong energy loss at the first time steps can be compensated and the turbulent kinetic energy is in the range of the reference case after reaching the equilibrium state.

The longitudinal and transverse correlations of the initialized HIT fields are plotted in Fig. 9. It can be seen that the results are similar for the longitudinal and transverse correlation for both FN and DN. The longitudinal correlations are strongly overpredicted for short distances (approximately up to $r/M = L_{\mathrm{int}}/M$) and under-

predicted for longer distances. Observing the energy spectra it was confirmed that both approaches do only provide large scale turbulence. In the three-dimensional flow fields, like shown in Fig. 10, these large structures can be identified as uniformly colored regions. In this figure one of the three velocity components of the initialized flow fields is shown for DN (left), FN (middle) and the NRC (right). It is seen that each structure does have an almost uniform velocity for FN and DN. Hence, the correlation is strong in the range up to the integral length scale. In the HIT field investigated experimentally also small structures are contained in the flow field. These structures might dampen out the correlation in the near field. Since they are equally distributed in the domain, the correlation in the far field is stronger for the experimental data than for FN and DN. Since the neighboring structures differ relatively strongly for FN and DN their velocity correlation is underpredicted for $r/M > L_{\mathrm{int}}/M$. The transverse correlations only match the experiments at large r/M, but they are overpredicted in the near field. This can be explained similarly to the longitudinal correlation. The dashed lines in Fig. 9 indicate the model correlation, which is used by the FN and DN generators. It is pointed out that the implemented algorithms for FN and DN provide velocity fields at the desired correlation, which however does not match the expected correlation for homogeneous isotropic turbulence. In Fig. 11 the temporal evolution of the different correlations is seen for the different grids. Compared to the NRC slight differences in the temporal behavior of the correlation can be revealed. A uniform growth across the considered range would be expected, as illustrated by the experimental data points. However for FN and DN it is observed that the correlation reduces for short distances at the first time interval, which results in a better fit with experimental data. The small growth rates comparing $\tilde{t} = 56$ and $\tilde{t} = 129$ were also observed for the reference case and seem to be no result of turbulence generation per se but of the overall numerical model.

4.3. Inverse Fourier approach

In this section, the results of the IF algorithm will be presented. Since the basic theory is the same, the temporal evolution of the energy spectra for IF is comparable to those of the NRC. The experimental data are matched well at all instants of time (Fig. 12). Only slight fluctuations occur for the smallest scales in the initial spectrum, which however disappear during decay.

The temporal evolution of the total kinetic energy fits the data of the NRC well. Only for grid III a slight underprediction is observed (Fig. 13). Similar observations are made for the subgrid scale viscosity. Indeed the experimental data are not

matched exactly but the time decay in the simulation confirms the expected results in principle. Comparing the energy spectra and the total kinetic energy for FN and DN as well as the Fourier based approaches it can be argued that the differences become negligible during decay. It is found out that k differs by no more than 20 percent comparing the inflow generators to the NRC. This seems to be relatively high but considering e.g. a turbulence intensity of ten percent for a nozzle outlet, an overprediction of 20 percent in the fluctuations would lead to an overprediction of about two percent in the turbulence intensity. Since the turbulence intensity is only an estimation, there is a small uncertainty in determining the exact boundary conditions, which can only be overcome with measurements that provide exact values for the fluctuations at the nozzle exit. The energy spectra for the inflow generators and the NRC at $\tilde{t} \approx 190$ are depicted in Fig. 14. It is obvious that the final velocity fields have approximately the same spectral content. The underprediction in the low wave number range and the overprediction in the high wave number range for FN and DN probably occur due to loss in kinetic energy and lower subgrid scale dissipation during the first time steps respectively.

In Fig. 15 the longitudinal velocity correlations are shown. In general the same observations are made as for the NRC. The correlations of the initialized HIT fields do not match the experimental data exactly but especially for the finer grid resolutions the general temporal evolution is well captured and again similar to the reference case. Similar conclusions can be drawn for the transverse correlation functions, which are not depicted here.

4.4. Discussion

The characteristics of the generated velocity fields were investigated and two different types were found. The first type contains turbulent structures at a given length scale where only the integral scales are included (FN, DN). Contrary to that the Fourier based approaches (NRC, IF) are able to generate fluctuations for all length scales of a specific energy spectrum. Despite the initial deficiencies for FN and DN, it could be shown that the spectral content of the flow fields becomes physical during the decay of turbulent structures, see Figs. 6 and 14. In the authors' opinion the time needed for converging to an equilibrium state cannot simply be transferred from the investigated HIT case to other test cases because it might be sensitive to the general flow characteristics. The turbulent kinetic energy of the initialized flow fields is not stringently the same for the different turbulence generators as discussed in Sec. 4.2. Thereby the following issues have to be considered when using the different

generators:

- Using FN or DN always includes the prescribed amount of kinetic energy in the resolved flow field independently of the grid resolution. Additionally considering the subgrid scale kinetic energy provided by the LES model leads to an overprediction of k_{tot} on coarse grids.

- Enforcing continuity by the pressure correction of the numerical solver removes the energy excess. However this may lead to an underprediction of the kinetic energy. Applying a precursor pressure correction in the generation procedure (after Lund's transformation) can ensure continuity for the generated velocity field. However rescaling the pressure corrected field by applying Lund's transformation for a second time was found to reintroduce divergence in the field.

- For IF only that amount of the prescribed kinetic energy is initialized, which corresponds to the resolved part of the energy spectrum. Since the algorithm ensures a solenoidal velocity field, no loss in the kinetic energy is induced by the pressure correction.

Some other aspects need to be considered for the evaluation of the turbulence generators. The FN algorithm is very easy to implement at a low computational cost due to the simplicity of the mathematical representation of the filter operation [Klein et al., 2003]. Similar assertions can be drawn for the DN approach which can be applied on arbitrary grids. Since diffusion is provided in almost any CFD code the implementation is straightforward. Moreover, the scaling of the length scale in the vicinity of solid walls can be reproduced [Kempf et al., 2005]. For the present case IF produces the most suitable energy spectra. However, it has to be considered that the energy spectrum is only a statistical interpretation of the discretized velocity field and that this is not necessarily an evidence for realistic turbulent structures. Vector plots of turbulent fields created by the three different inflow generators are shown in Fig. 16. It is seen that there is a wider range of differently sized structures for the IF approach when compared to FN and DN which confirms the findings from the energy spectra. Since all the synthetically generated turbulence fields contain large uniform structures, the fluctuations are not dissipated instantly and realistic vortex tubes can develop from the synthetic structures. Moreover plots of the λ_2-criterion are depicted in Fig. 16. The λ_2-criterion indicates the presence of vortices if $\lambda_2 < 0$ is satisfied and it is defined as the intermediate eigenvalue of the sum of the squared strain-rate and vorticity tensors Haller [2005]. It is seen in these plots that for the IF approach small coherent vortex structures are contained in the flow field, which

again confirms the previous findings. For FN and DN we here observe mainly large structures which qualitatively corresponds to the spectral analyses conducted.

5. Conclusion and outlook

The aim of the present work was to evaluate different methods for generating turbulent inflow data for the Large Eddy Simulation of turbulent flows. Three different techniques were investigated. Digital filtering (FN) of random data is used in the first approach. In this way large scale structures are generated from the random data. The application of a diffusion operation affects white noise in a similar way and is used as second inflow generation method (DN). Both FN and DN create spatial correlations in initially fully randomized data fields. The third algorithm makes use of a prescribed energy spectrum function (IF). The fluctuation field is obtained from a Fourier series.

In the considered test case velocity fields are created in a cubical domain with each turbulence generation method. The decay of the fluctuations in time was investigated by comparing the results to experimental data. The results revealed two different categories of inflow generators. FN and DN are of the first kind providing mainly large scale structures. The energy spectrum is not fully represented due to the missing small scale turbulence. However, it is shown that the energy overprediction at the large scales is reduced by generating small scale turbulence during the decay leading to a physically correct energy spectrum. Similar observations are made for the velocity correlations, which are not perfectly predicted for the initialized fields but which reach a more physical state during the decay. IF is of the second type, generating eddies at all resolved length scales and representing the energy spectrum even for the initialized field. The decay is well predicted compared to the experimental data. In general it can be concluded that each generator is able to create fluctuations at a desired integral length scale and root-mean-square velocity. Coming back to the questions raised in section 1, the following conclusions can be drawn from the present investigation:

- The characteristic energy spectrum for homogeneous isotropic turbulence is fully represented for IF. FN and DN do only provide large scale turbulence.
- The velocity correlations are well reproduced for IF. The model correlation prescribed for FN and DN does not compare well to the experimental values initially.

- The turbulent statistics are well predicted for IF comparing numerical and experimental data. The discrepancies observed in the initialized velocity fields for FN and DN vanish during the decay of turbulence. Both the energy spectra and the velocity correlations become physically meaningful and compare well to experimental data despite the initial differences.

- A desired length scale and turbulence intensity can be reproduced by the different algorithms. The present configuration provides information on turbulent characteristics and related properties for different turbulence generation methods.

The HIT case is the most generic test case for the investigation of turbulence and here, it gives us a deeper insight in the characteristics of the generated velocity fields and thereby in the potentials of the different inflow generators considered. However it has to be kept in mind that this test case is not the usual application concerning the actual scope of the inflow generators. Hence, in future investigations, the results and methods from the present work will be applied in a comparative fashion for realistic test cases such as anisotropic jet flows.

Acknowledgement

The authors gratefully acknowledge funding by the Federal Ministry of Education and Research of Germany in the framework of Virtuhcon (project number 03Z2FN11).

References

Klein, M., Sadiki, A., Janicka, J.. A digital filter based generation of inflow data for spatially developing direct numerical or large eddy simulations. Journal of Computational Physics 2003;186(2):652 – 665.

Kempf, A., Klein, M., Janicka, J.. Efficient generation of initial- and inflow-conditions for transient turbulent flows in arbitrary geometries. Flow, Turbulence and Combustion 2005;74:67 – 84.

Billson, M., Eriksson, L.E., Davidson, L.. Jet noise prediction using stochastic turbulence modeling. In: 9th AIAA/CEAS Aeroacoustic Conference 2003. 2003,.

Davidson, L.. Using isotropic synthetic fluctuations as inlet boundary conditions for unsteady simulations. Advances and Applications in Fluid Mechanics 2007a;1:1–35.

Bordas, R., John, V., Schmeyer, E., Thevenin, D.. Measurment and simulation of a droplet population in a turbulent flow field. Computers & Fluids 2012;66:52–62.

Bini, M., Jones, W.. Large-eddy simulation of particle-laden turbulent flows. Journal of Fluid Mechanics 2008;614:207–252.

Kuenne, G., Seffrin, F., Fuest, F., Stahler, T., Ketelheun, A., Geyer, D., et al. Experimental and numerical analysis of a lean premixed stratified burner using 1d raman/rayleigh scattering and large eddy simulation. Combustion and Flame 2012;159:2669–2689.

Enjalbert, N., Domingo, P., Vervisch, L.. Mixing time-history effects in large eddy simulation of non-premixed turbulent flames: Flow-controlled chemistry tabulation. Combustion and Flame 2012;159:336–352.

Duwig, C.. Large eddy simulation of flame stabilisation dynamics and vortex control in a lifted h2/n2 jet flame. Combustion Theory and Modelling 2011;15:325–346.

Rhea, S., Bini, M., Fairweather, M., Jones, W.. Rans modelling and les of a single-phase, impinging plane jet. Computers and Chemical Engineering 2009;33:1344–1353.

Olbricht, C., Stein, O., Janicka., J., van Oijen, J., Wysocki, S., Kempf, A.. Les of lifted flames in a gas turbine model combustor using top-hat filtered pfgm chemistry. Fuel 2012;96:100–107.

Pettit, M., Coriton, B., Gomez, A., Kempf, A.. Large-eddy simulation and experiments on non-premixed highly turbulent opposed jet flows. Proceedings of the Combustion Institute 2011;33:1391–1399.

Fru, G., Thevenin, D., Janiga, G.. Impact of turbulence intensity and equivalence ratio on the burning rate of premixed methane-air flames. Energies 2011;4:878–893.

Stein, O., Böhm, B., Dreizler, A., Kempf, A.. Highly-resolved les and piv analysis of isothermal turbulent opposed jets for combustion applications. Flow, Turbulence and Combustion 2011;87:425–447.

Piscaglia, F., Montorfano, A., Onorati, A., Brusiane, F.. Boundary conditions and subgrid scale models for les simulation of ic engines. *in proceedings* of "Oil & Gas Science and Technology" 2013;.

Huang, S., Li, Q., Wu, J.. A general inflow turbulence generator for large eddy simulation. Journal of Wind Engineering and Industrial Aerodynamics 2010;98:600–617.

Jarrin, N., Benhamadouche, S., Laurence, D., Prosser, R.. A synthetic-eddy-method for generating inflow conditions for large-eddy simulations. International Journal of Heat and Fluid Flow 2006;27:585–593.

Montomoli, F., Eastwood, S.. Implementation of synthetic turbulence inlet for turbomachinery les. Computers & Fluids 2011;46:369–374.

Baba-Ahmadi, M., Tabor, G.. Inlet conditions for les using mapping and feedback control. Computers & Fluids 2009;38:1299–1311.

Lee, S., Lele, S.K., Moin, P.. Simulation of spatially evolving turbulence and the applicability of taylors hypothesis in compressible flow. Physics of Fluids 1992;4:1521 – 1530.

Sohm, V.. Hybrid turbulence simulation to predict cyclic variations in internal combustion engines. Ph.D. thesis; Rhein-Westfälische Technische Hochschule Aachen; 2007.

Pronk, F.T., Hulshoff, S.J.. A comparison of inflow generation methods for large-eddy simulation. World Academy of Science, Engineering and Technology 2012;68:1575–1580.

Tabor, G., Baba-Ahmadi, M.. Inlet conditions for large eddy simulation: A review. Computers & Fluids 2010;39(4):553 – 567. doi:10.1016/j.compfluid.2009.10.007. URL http://www.sciencedirect.com/science/article/pii/S0045793009001601.

Versteeg, H., Malalasekera, W.. An Introduction to Computational Fluid Dynamics - The Finite Volume Method. Pearson Education Limited; 2007.

Fröhlich, J.. Large Eddy Simulation turbulenter Strömungen. B.G. Teubner Verlag Wiesbaden; 2006.

Batchelor, G.. The Theory of Homogeneous Turbulence. Cambridge: Cambridge University Press; 1953.

Lund, T.S., Wu, X., Squires, K.D.. Generation of turbulent inflow data for spatially-developing boundary layer simulations. Journal of Computational Physics 1998;140:233 – 258.

Kempf, A., Wysocki, S., Pettit, M.. An efficient, parallel low-storage implementation of kleins turbulence generator for les and dns. Computers & Fluids 2012;60(0):58 – 60. doi:10.1016/j.compfluid.2012.02.027. URL http://www.sciencedirect.com/science/article/pii/S0045793012000825.

Kraichnan, R.H.. Diffusion by a random velocity field. Physics of Fluids 1970;13:22–31.

Davidson, L.. Hybrid les-rans: Inlet boundary conditions for flows including recirculation. In: 5th International Symposium on Turbulence and Shear Flow Phenomena TU Munich. 2007b,.

Pope, S.B.. Turbulent Flows. Cambridge University Press; 2000.

Moin, P., Squires, K., Cabot, W., Lee, S.. A dynamic subdrid-scale model for compressible turbulence and scalar transport. Physics of Fluids 1991;3:2746 – 2757.

Fureby, C., Tabor, G., Weller, H., Gosman, A.. A comparative study of subgrid scale models in homogeneous isotropic turbulence. Physics of Fluids 1997;9:1416 – 1429.

Nicoud, F., Ducros, F.. Subgrid-scale stress modelling based on the square of the velocity gradient tensor. Flow, Turbulence and Combustion 1999;62:183–200.

Hasse, C., Sohm, V., Wetzel, M., Durst, B.. Hybrid URANS/LES turbulence simulation of vortex shedding behind a triangular flameholder. Flow, Turbulence and Combustion 2009;83(1):1–20.

Nicoud, F., Toda, H.B., Cabrit, O., Bose, S., Lee, J.. Using singular values to build a subdrid-scale model for large eddy simulations. Physics of Fluids 2011;23:1 – 12.

Comte-Bellot, G., Corrsin, S.. Simple eulerian time correlation of full- and narrow-band velocity signals in grid-generated, isotropic turbulence. Journal of Fluid Mechanics 1971;48:237 – 337.

Haller, G.. An objective definition of a vortex. Journal of Fluid Mechanics 2005;525:1–26.

Tables

Table 1: Parameters for the flow field initialization according to the experimental data of Comte-Bellot and Corrsin Comte-Bellot and Corrsin [1971] at $\tilde{t} = 42$

quantity	value	unit
u_{rms}	0.222	m/s
ε	0.474	m^2/s^3
L_{int}	0.024	m
η	0.00029	m

Table 2: Grid spacing and time step width

Grid	Number of grid elements	Δx [m]	Δt [s]
I	64^3	0.0079375	0.0005
II	128^3	0.00396875	0.0002
III	256^3	0.001984375	0.0001

Figures

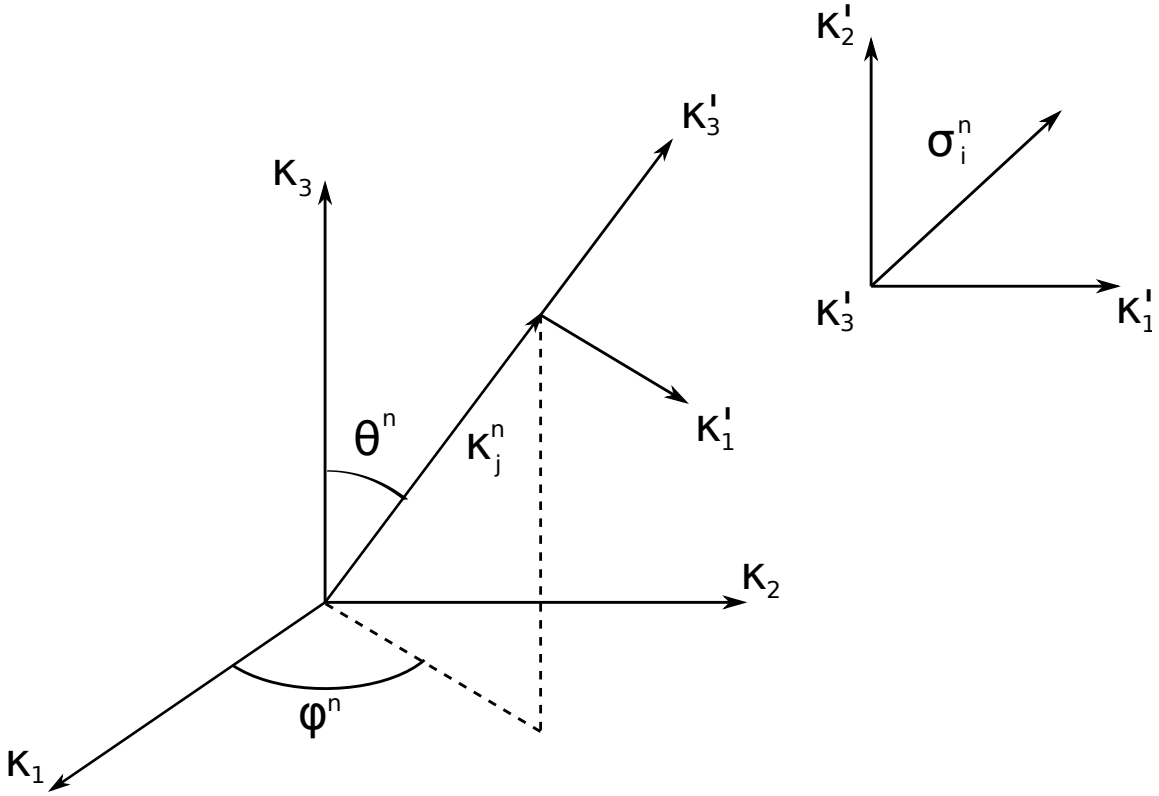

Figure 1: Geometric convention for definition of wave number vector κ_j^n and unit vector σ_i^n.

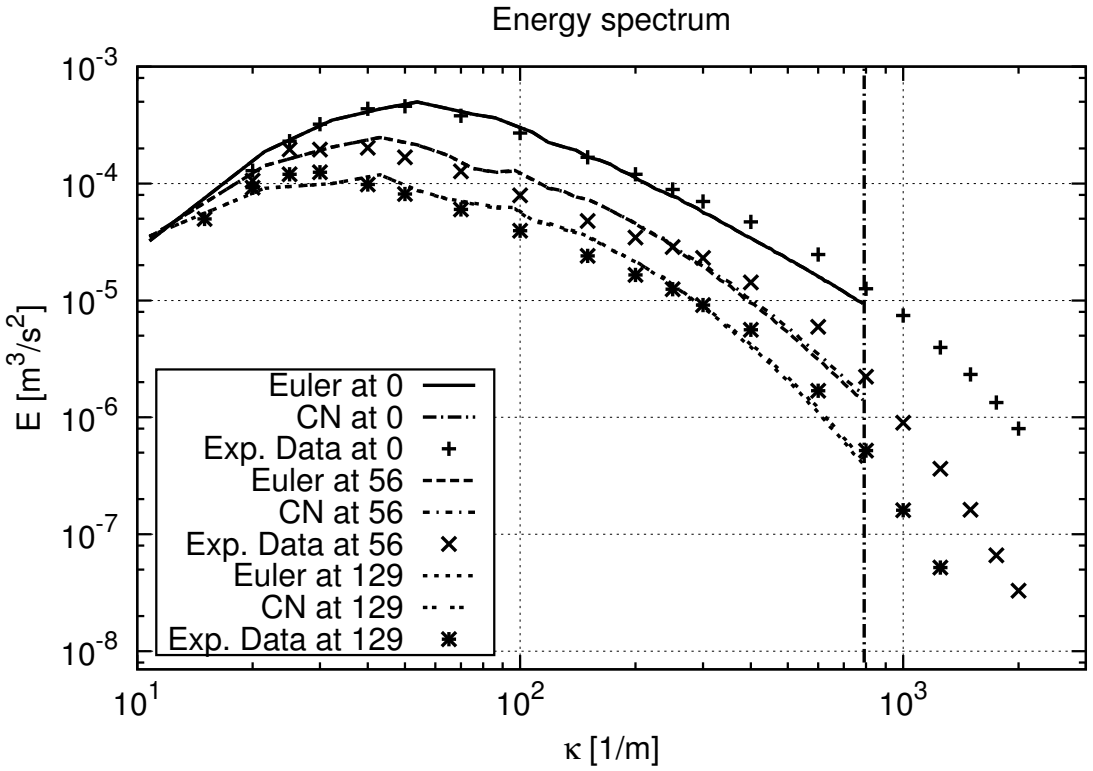

Figure 2: Energy spectra during decay of turbulence in a box for NRC with using first order Euler scheme and second order Crank-Nicolson scheme (CN) for time discretization.

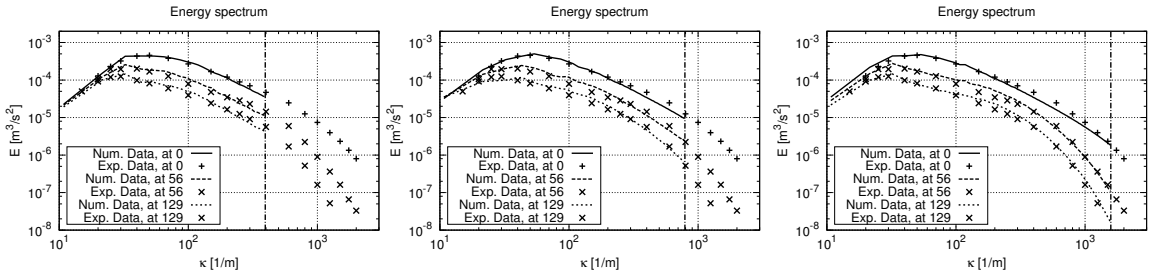

Figure 3: Energy spectra during decay of turbulence in a box for NRC. Left: Grid I (64^3 cells, $C_s = 0.17$); Middle: Grid II (128^3 cells, $C_s = 0.14$); Right: Grid III (256^3 cells, $C_s = 0.14$).

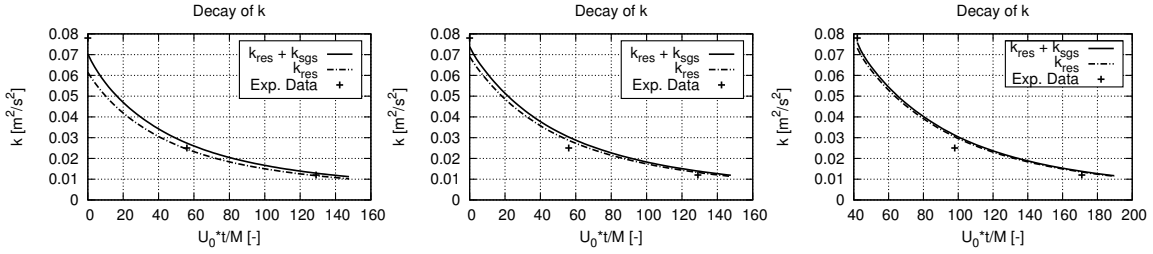

Figure 4: Decay of resolved and total turbulent kinetic energy in a box for NRC. Left: Grid I (64^3 cells, $C_s = 0.17$); Middle: Grid II (128^3 cells, $C_s = 0.14$); Right: Grid III (256^3 cells, $C_s = 0.14$).

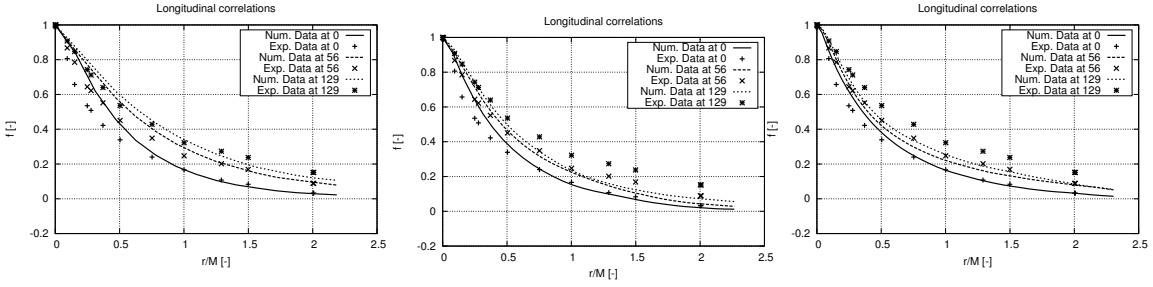

Figure 5: Evolution of longitudinal velocity correlation for NRC. Left: Grid I (64^3 cells, $C_s = 0.17$); Middle: Grid II (128^3 cells, $C_s = 0.14$); Right: Grid III (256^3 cells, $C_s = 0.14$).

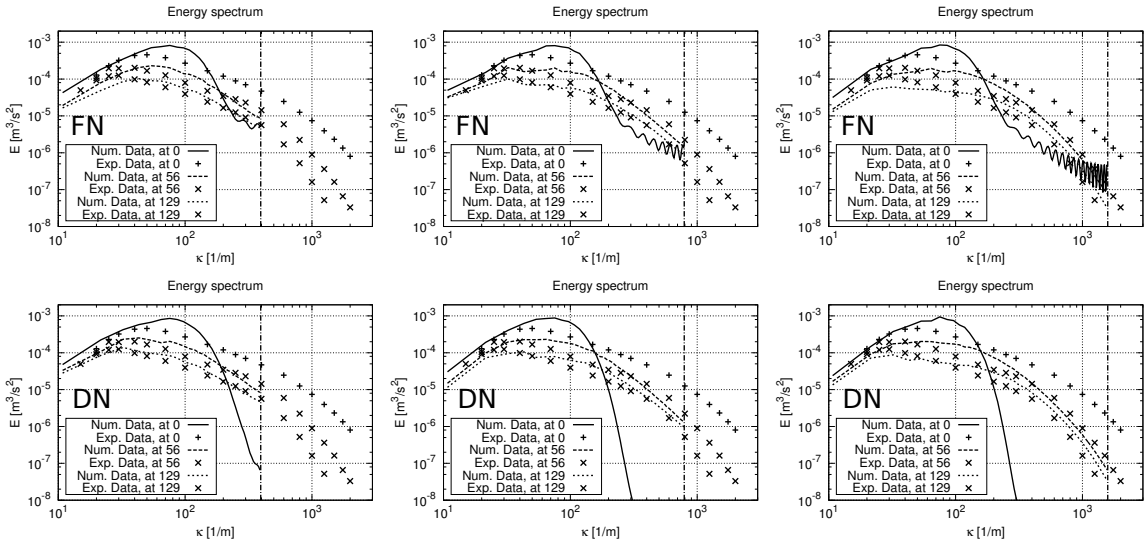

Figure 6: Energy spectra from FN (top) and DN (bottom) during decay for different meshes; Left: Grid I (64^3 cells, $C_s = 0.17$); Middle: Grid II (128^3 cells, $C_s = 0.14$); Right: Grid III (256^3 cells, $C_s = 0.14$).

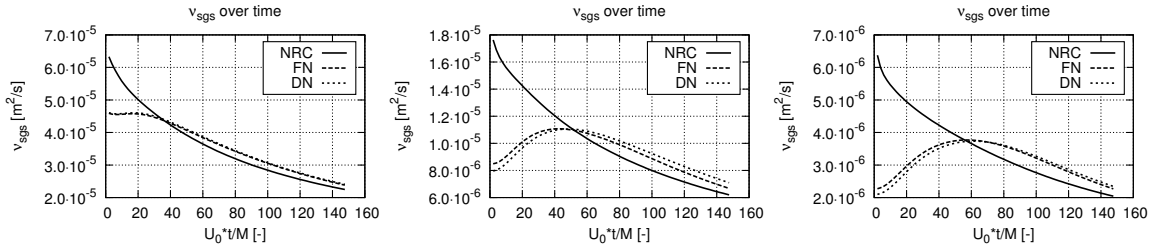

Figure 7: Subgrid scale viscosity during decay of turbulence on different meshes; Left: Grid I (64^3 cells, $C_s = 0.17$); Middle: Grid II (128^3 cells, $C_s = 0.14$); Right: Grid III (256^3 cells, $C_s = 0.14$).

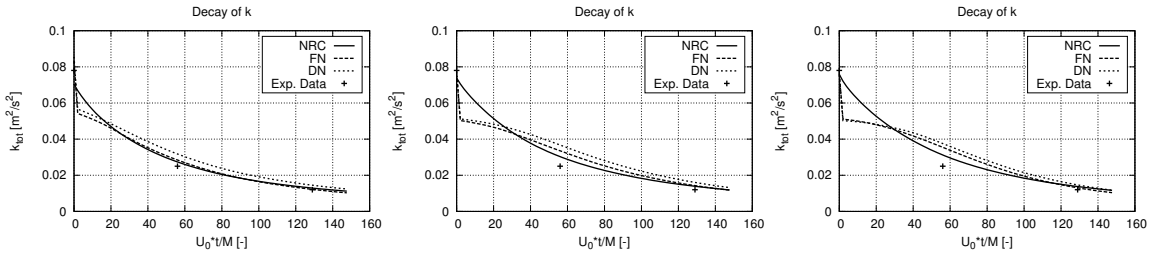

Figure 8: Temporal evolution of total kinetic energy for inverse Fourier transformation, FN, DN, and experiments; Left: Grid I (64^3 cells, $C_s = 0.17$); Middle: Grid II (128^3 cells, $C_s = 0.14$); Right: Grid III (256^3 cells, $C_s = 0.14$).

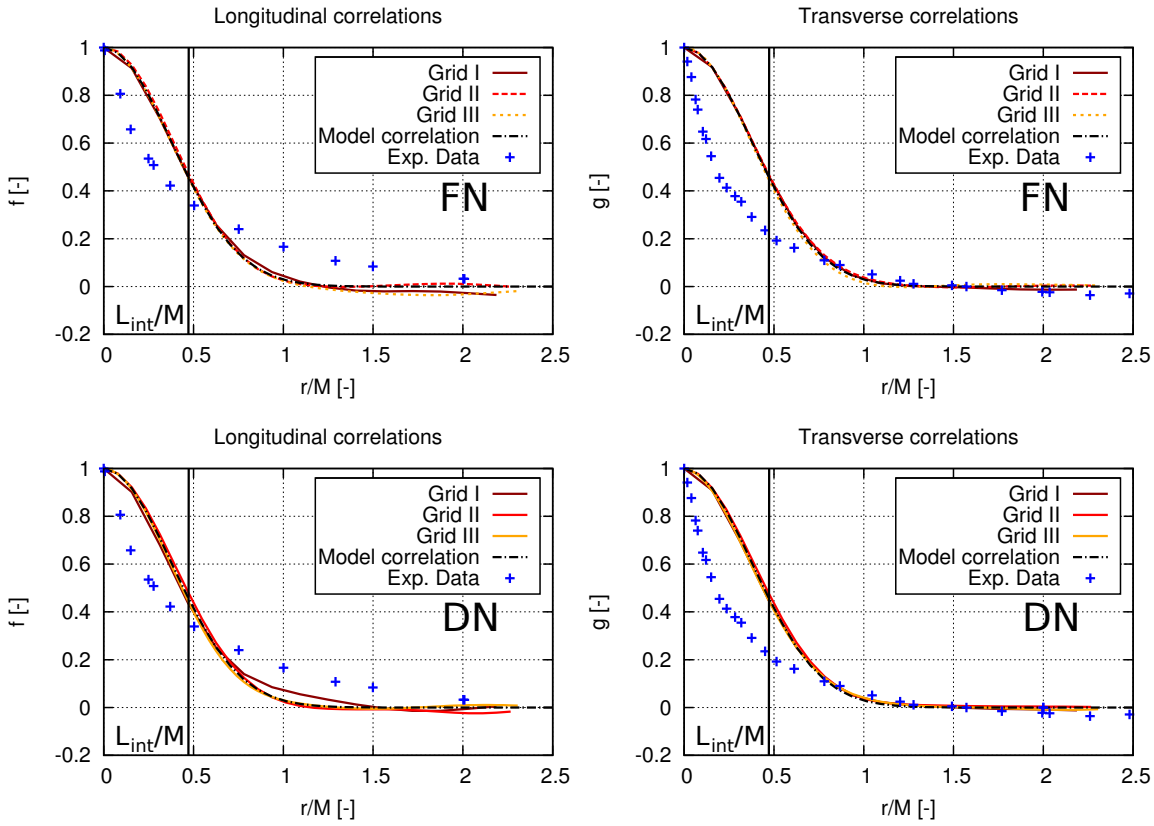

Figure 9: Longitudinal (left) and transverse (right) velocity correlations of initialized turbulence fields for FN (top) and DN (bottom).

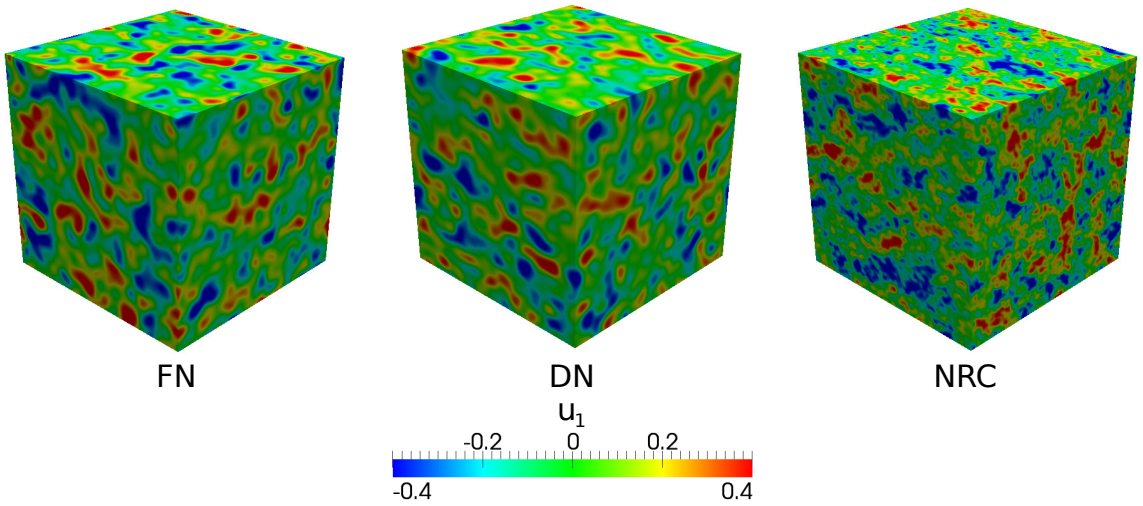

Figure 10: x-component of initial cubical velocity fields for FN (left), DN (middle) and NRC (right) on grid II

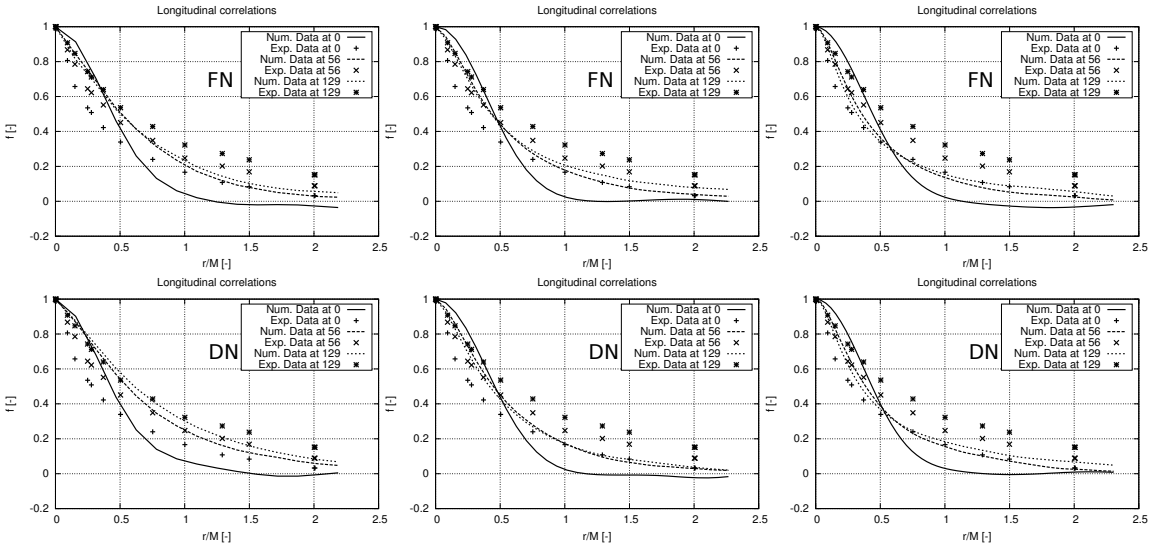

Figure 11: Temporal evolution of longitudinal velocity correlation for FN (top) and DN (bottom); Left: Grid I (64^3 cells, $C_s = 0.17$); Middle: Grid II (128^3 cells, $C_s = 0.14$); Right: Grid III (256^3 cells, $C_s = 0.14$).

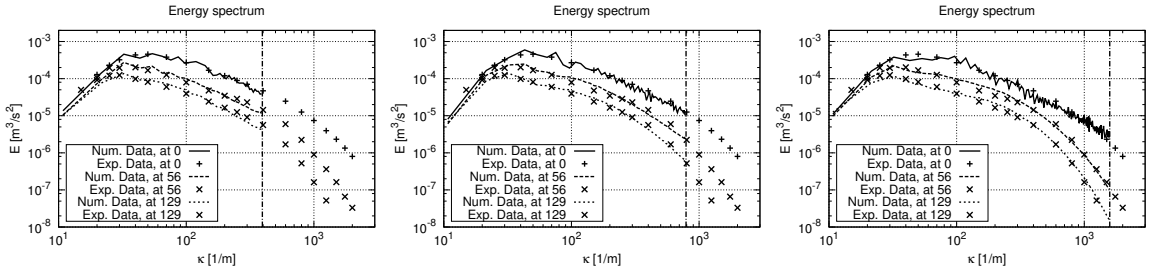

Figure 12: Energy spectra from IF during decay for different meshes; Left: Grid I (64^3 cells, $C_s = 0.17$); Middle: Grid II (128^3 cells, $C_s = 0.14$); Right: Grid III (256^3 cells, $C_s = 0.14$).

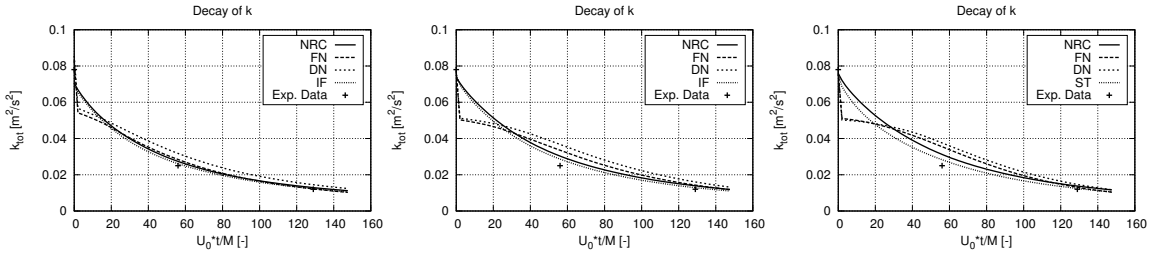

Figure 13: Temporal evolution of total kinetic energy for NRC, FN, DN, IF and experiments; Left: Grid I (64^3 cells, $C_s = 0.17$); Middle: Grid II (128^3 cells, $C_s = 0.14$); Right: Grid III (256^3 cells, $C_s = 0.14$).

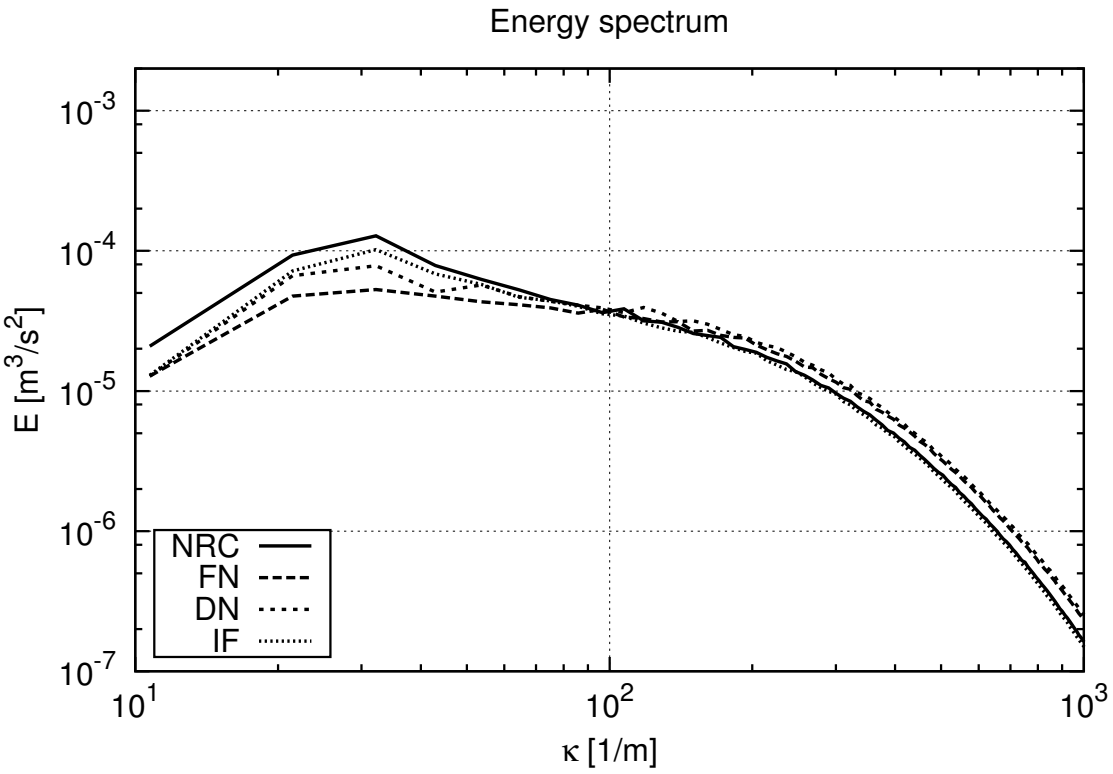

Figure 14: Energy spectra at the last instant of time ($t = 0.75$ s) for grid III (256^3 cells).

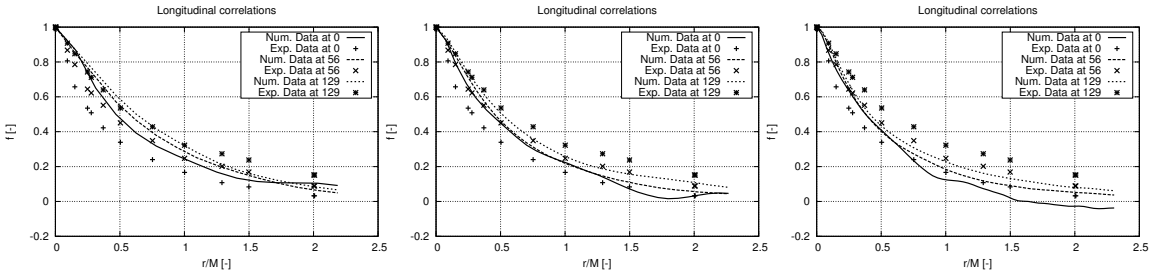

Figure 15: Temporal evolution of longitudinal velocity correlation for IF; Left: Grid I (64^3 cells, $C_s = 0.17$); Middle: Grid II (128^3 cells, $C_s = 0.14$); Right: Grid III (256^3 cells, $C_s = 0.14$).

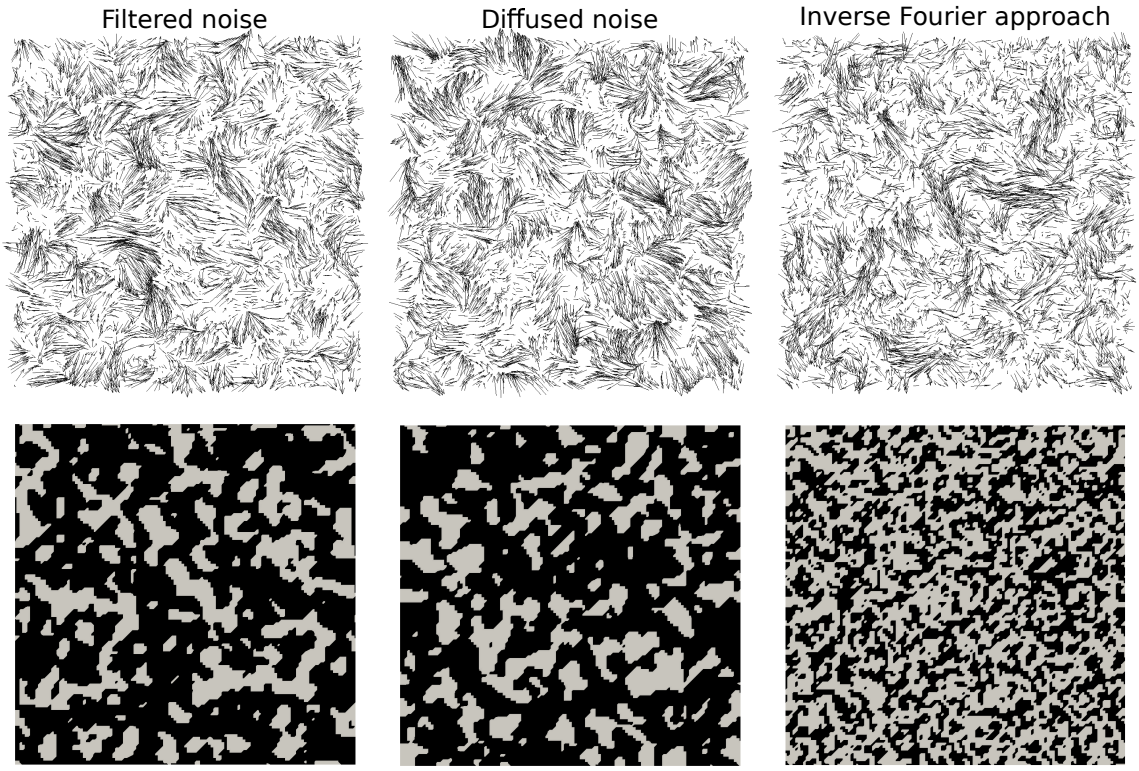

Figure 16: Velocity vectors (top) and λ_2-criterion (bottom) of the initialized turbulent fields for FN (left), DN (middle) and IF (right). Black areas in λ_2-plot indicate $\lambda_2 < 0$.